Relating Hydraulic-Electrical-Elastic Properties of Natural Rock Fractures at Elevated Stress and Associated Transient Changes of Fracture Flow

K. Sawayama[1], T. Ishibashi[2], F. Jiang[3,4,6], T. Tsuji[4,5,7] and Y. Fujimitsu[5]

[1]Department of Earth Resources Engineering, Graduate school of Engineering, Kyushu University, Fukuoka, Japan.

[2]Fukushima Renewable Energy Institute, National Institute of Advanced Industrial Science and Technology, Koriyama, Japan.

[3]Department of Mechanical Engineering, Graduate school of Sciences and Technology for Innovation, Yamaguchi University, Ube, Japan.

[4]International Institute for Carbon-Neutral Energy Research, Kyushu University, Fukuoka, Japan.

[5]Department of Earth Resources Engineering, Faculty of Engineering, Kyushu University, Fukuoka, Japan.

[6]Blue energy center for SGE technology (BEST), Yamaguchi University, Ube, Japan

[7]Disaster Prevention Research Institute, Kyoto University, Uji, Japan

Corresponding author: Kazuki Sawayama (k.sawayama0926@mine.kyushu-u.ac.jp)

Key Points:

- Changes in permeability and resistivity with stress depend on connectivity; changes in velocity with stress depend on asperity contacts.
- Resistivity can be linked with permeability and flow area regardless of fracture roughness, whereas velocity has roughness dependence.
- Transitions of fracture flow patterns with stress define three stages that may be evident in remotely measured geophysical properties.

Abstract

Monitoring the hydraulic properties within subsurface fractures is vitally important in the contexts of geoengineering developments and earthquakes. Geophysical observations are promising tools for remote determination of subsurface hydraulic properties; however, quantitative interpretations are hampered by the paucity of relevant geophysical data for fractured rock masses. This study explored simultaneous changes in hydraulic and geophysical properties of natural rock fractures with increasing normal stress and correlated these property changes through coupling experiments and digital fracture simulations. We show that electrical resistivity is linked with permeability and flow area regardless of fracture roughness, whereas elastic wave velocity is roughness dependent. We also are able to categorize fracture flow patterns as aperture-dependent, aperture-independent, or disconnected flows, with transitions at specific stress levels. Elastic wave velocity offers potential for detecting the transition between aperture-dependent flow and aperture-independent flow, and resistivity is sensitive to detect the connection/disconnection of the fracture flow.

Plain Language Summary

Monitoring the flow of fluids through underground fractures is important for developing earth resources or predicting earthquakes. This can be done by observing physical properties underground, but it is poorly understood how geophysical and hydraulic properties are related because we have limited data from rock fractures. In this study, we explored changes in hydraulic and geophysical properties of natural rock fractures by subjecting rock specimens to increasing normal stress in laboratory experiments and in numerical simulations of digital rock fractures. We learned that electrical resistivity is linked to fracture permeability and flow area regardless of fracture roughness changes, whereas elastic wave velocity depends on roughness. We were able to classify different patterns of fracture flow into three stages: aperture-dependent flow, aperture-independent flow, and disconnected flow. Elastic wave velocity changes can indicate the change between the first two stages, and resistivity can do the same for the last two.

1 Introduction

The hydraulic properties of fractured geological formations have been of interest for many purposes such as fluid resources (e.g., geothermal fluids, shale oil and groundwater), geological storage or disposal, and seismic events (fault reactivation and induced seismicity). It is known that fracture permeability and preferential flow paths within fractures are controlled by the heterogeneous distribution of apertures, which can vary as stress changes (Raven & Gale, 1985; Watanabe et al., 2008; Ishibashi et al., 2015; Chen et al., 2017; Vogler et al., 2018). In-situ stress is never constant during geoengineering developments or on the geological time scale, and consequently the aperture distribution and associated hydraulic properties also must change in natural settings. These changes produce transitions in the patterns of fracture flow that in turn control the fault reactivation cycle (Sibson et al., 1988) and characterize the transport behavior of fluid resources.

Geophysical observations can detect changes in electrical resistivity or elastic wave velocity that may reflect subsurface stress changes associated with hydraulic stimulation, earthquakes or geothermal fluid production (Peacock et al., 2012, 2013; Didana et al., 2017; Nimiya et al., 2017; Taira et al., 2018). It would be beneficial if changes in aperture-related hydraulic properties triggered by subsurface stress changes could be linked to geophysical properties that can be remotely monitored. Studies based on synthetic single fractures have related

hydraulic properties to electrical properties (Brown, 1989; Kirkby et al., 2016) and to elastic properties (Pyrak-Nolte & Nolte, 2016; Wang & Cardenas, 2016). These studies have revealed that hydraulic and electrical properties are dependent on fluid connectivity whereas elastic properties are dependent on asperity contacts, and although all of these dependencies are related to fracture geometry, they do not necessarily have a mutual correlation. Simultaneous measurements in identical samples may shed light on the nature of variations in rock properties; however, to our knowledge no study has simultaneously investigated hydraulic, electrical and elastic properties of natural rock fractures. This study took advantage of recent advances in digital modeling of rock physics (e.g., Tsuji et al., 2019; Sain et al., 2014) that enabled us to simultaneously determine multiple properties in the same sample while visualizing its microstructure.

In this study, we explored the simultaneous changes in fracture permeability, electrical resistivity and elastic wave velocity of natural rock fractures that occur with increasing normal stress. By coupling experiments and digital fracture simulations, we investigated the correlations between these properties and addressed their governing mechanisms. In this paper, we also evaluate the local behavior of the fluid flow (i.e., preferential flow paths) within fractures to investigate the connectivity of flow paths, flow area and their transient changes. Our lattice Boltzmann simulation of digitized rock fractures reveals transitions in 3D fracture flow patterns that accompany stress changes, which are difficult to observe in laboratory experiments or in the field. We discuss how transient changes of the fracture flow pattern are correlated with hydraulic and geophysical properties and suggest possible applications of our findings to seismogenic zones and geothermal reservoirs.

2 Methods

We evaluated the dependency of the fracture permeability on the effective normal stress via the fluid flow experiments. These employed two cylindrical fractured samples of Inada granite 50 mm in diameter and 80 mm long, in which the fracture plane was parallel to the central axis. The two samples differed in the roughness characteristics of their fracture surfaces (*smooth*/*rough*), as determined from the surface topographies of the hanging wall and footwall which we mapped in a grid of cells 23.433 μm square with a 3D measuring microscope (Keyence, VR-3050). The surface of one sample (smooth), had a fractal dimension D of 2.5 and a root mean square height (RMSH) of 1.3 mm, whereas the surface of the other sample (rough) had D=2.4 and RMSH=1.7 mm (Power et al., 1987; Power & Durham, 1997). We performed fluid flow experiments on these two samples under various effective normal stresses between 5 and 30 MPa. For each stress state, we evaluated the fracture permeability based on the cubic law, where we assumed Darcy flow and a negligible matrix permeability of granite (between 10^{-19} and 10^{-22} m^2).

Subsequently, we simulated 3D fracture flows with the lattice Boltzmann method, which is suitable for modeling heterogeneous local flows with complex boundaries (He & Luo, 1997; Jiang et al., 2014). We employed the multi-relaxation-time D3Q19 model (Ahrenholz et al., 2008), in which the fluid flow is driven by a constant body force from the inlet boundary to the outlet boundary (Figure S1). Bounce-back boundaries were implemented at the fracture surface and periodic boundary conditions were applied along the fracture plane. Three-dimensional digital fracture models were prepared for each sample in a 0.1 mm cubic system based on its surface topographies. The distance between the two surfaces was adjusted in each model so that the digital fracture had a simulated permeability equivalent to that measured in the real fracture (Watanabe

et al., 2008; Ishibashi et al., 2015). A series of lattice Boltzmann simulations enabled us to explore the changes with stress state in fracture permeability and in the flow area, defined as the ratio of the area of preferential flow paths to the area of the fracture plane.

Once the lattice Boltzmann simulations yielded estimates of the heterogeneous distribution of flow within the fracture, we evaluated both the resistivity and the elastic wave velocity by using the finite-element method (Garboczi, 1998; Andrä et al., 2013; Saxena & Mavko, 2016). Resistivity was calculated from a simulated electric current and the potential difference associated with the applied voltage parallel to the fluid flow direction. Elastic wave velocity in the direction perpendicular to the fracture plane was estimated from the simulated static elasticity (low-frequency limit) under the triaxial stress state. Parameters used in our finite-element modeling are summarized in Table 1.

3 Results and Discussion

3.1 Changes in fracture permeability and preferential flow with aperture closure

Our digital fracture simulations closely reproduced our experimental results for the smooth (Figure 1a) and rough (Figure 1b) surfaces. Plots of the logarithmic permeability against stress show a change with increasing effective normal stress from curving trends to linear trends. Figures 1c and 1d show representative simulation results for the distribution of apertures (in grayscale) and associated flow rates (in color) through the smooth and rough fractures, respectively. Note that the flows in Figure 1 represent the summation of flow rates in every z-direction (perpendicular to the fracture plane), normalized with respect to their maximum value. Regions with >1% of the maximum flow rate are colored to accentuate the dominant flow paths. At low stresses, preferential flow paths form that cover most of the area with open (non-zero) apertures (images i in Figure 1). Isolated apertures also form, few at first, that are surrounded by contacting asperities (zero aperture points), where the fluid is stagnant (white patches in Figures 1c and 1d).

As stress increases, larger fractions of the fracture surfaces are in contact, and hence the dominant flow paths decrease in number. As the dominant flow paths become less significant, flow paths from the inlet to outlet are progressively disconnected (images iii and iv in Figure 1). Accordingly, the permeability-stress relationship includes a transition: logarithmic permeability changes exponentially with stress while flow paths are connected (images i and ii) and linearly while flow paths are disconnected (images iii and iv). The stress level where this change occurs can be defined as the hydraulic percolation threshold σ_{HPT}, which signifies the creation of continuous flow paths through rocks (Guéguen et al., 1997; Kirkby et al., 2016). Roughness does not appear to greatly affect this threshold.

3.2 Relations of hydraulic and geophysical properties

We present the evolution of several rock properties with stress changes in Figure 2. Note that we discuss only P-wave velocity here as P- and S-wave velocities show similar tendencies. Fracture permeability and resistivity show a linear trend at stresses higher than σ_{HPT} but deviate from a linear trend at lower stresses, and neither property displays any dependence on fracture roughness (Figures 2a and 2b). As these two properties are generally sensitive to fluid connectivity (Guéguen & Palciauskas, 1994), we infer that connectivity is unlikely to change with differences in roughness. Elastic wave velocity varies notably with roughness, and unlike the case with porous rocks, there is no clear correlation between velocity and porosity (Figures 2c and 2d). As the P-

wave velocity difference (~340 m/s at ~1.2% of porosity) is explained in terms of the difference in contact area of the asperity (~17% at ~1.2% of porosity; Table S1), we conclude that both porosity and asperity contacts contribute to the velocity difference in rock fractures.

A further comparison shows that resistivity has a stable relationship with permeability on a log-log basis that does not vary with roughness (Figure 3a), which suggests that mechanisms underlying changes in resistivity and permeability are the same and do not depend on roughness. This relationship reflects the roughness independence of σ_{HPT}, as fluid connectivity is a key factor in characterizing changes in both permeability and resistivity (Figure 2). On the other hand, the relationship of P-wave velocity with logarithmic permeability is sensitive to roughness (Figure 3a).

The relationship between logarithmic resistivity and flow area is also insensitive to roughness (Figure 3b), reflecting the positive correlation between permeability and flow area (Zimmerman et al., 1992; Nemoto et al., 2009). The relationship between P-wave velocity and flow area is roughness-dependent when flow areas are below 60% but not so when flow areas exceed 60% (Figure 3b). The transition at ~60% flow area coincides with the mechanical percolation threshold, as discussed below.

3.3 Transitions in the fracture flow pattern and associated changes in geophysical properties

Although many experimental studies in intact rocks have revealed the evolution of rock properties with stress change (Brace & Orange, 1968; Scholtz, 2002; Paterson & Wang, 2005), some observations detected unusual changes of rock properties that cannot be explained by these experimental results (Park, 1991; Xue et al., 2013). The presence of mesoscale fractures may account for these discrepancies. To investigate this issue, we compiled our results on the evolution of rock properties in single fractures and compared them with the changes in flow rate distribution within the fracture. These changes in rock properties can be categorized as roughness-dependent (Figure 4a) or roughness-independent (Figure 4b).

Elastic wave velocity and flow area are both roughness-dependent, thus we can distinguish separate mechanical percolation thresholds for smooth fractures (σ_{MPT}) and rough fractures (σ'_{MPT}), defined in both cases as the stress at which velocity reaches 90% of its maximum value (Figure 4a). Because σ_{MPT} is smaller than σ'_{MPT}, velocity increases more sharply with stress in smooth fractures than in rough fractures. The difference arises from a discrepancy in the heterogeneous aperture distribution (Figure S2). The slower velocity change in rough fractures reflects the broader distribution of aperture sizes, which is considered to be analogous with velocity change in rock containing cracks of various aspect ratios (Tsuji et al., 2008; Mavko et al., 2009). Resistivity and permeability are both roughness independent (Figure 4b). Tendencies of these changes depend on the hydraulic percolation threshold σ_{HPT}, which is greater than σ_{MPT} (Guéguen et al., 1997).

Figure 4c schematically illustrates these changes in rock properties as three stages (Stage I–III) defined by transitions of the fracture flow pattern within a subsurface fracture with increasing stress. At lower stresses, Stage I represents *aperture-dependent flow*, where fluid flows within most of the area containing apertures and the flow area decreases as the mean aperture decreases (Figure 4a). Stage II, at stresses higher than σ_{MPT}, represents *aperture-independent flow*, in which isolated apertures appear and become areas without flow. In this stage, the flow area decreases markedly with increasing stress, exceeding the decrease in the mean aperture (Figure 4a). Although elastic wave velocity remains nearly constant, permeability and resistivity change exponentially

because there are still connected flows. In Stage III, at stresses higher than σ_{HPT}, flow paths become disconnected and result in *disconnected flow*. In this stage, logarithmic permeability and resistivity change linearly with stress and areas without flow become a significant fraction of the fracture area. Because Stage II begins when the velocity ceases to change with rising stress, the Stage I–II transition can be detected by velocity monitoring, whereas resistivity is sensitive to the Stage II–III transition. This means that, if monitoring detects the combination of almost constant velocity and exponential change in the logarithmic resistivity, it may signal the presence of aperture-independent (Stage II) flow.

If crustal stress can be considered constant (i.e., on relatively short timescales), then changes in the fracture flow pattern with changes in effective normal stress represent changes in pore pressure. This finding may show promise in two applications. One application involves the evolution of fluid flow along faults, which is part of the fault reactivation cycle triggered by pore pressure perturbations. Our model of Stage I reproduces observations of high permeability (Xue et al., 2013; Kinoshita et al., 2015), low resistivity (Mazzella & Morrison, 1974; Park, 1991) and low seismic velocity (Brenguier et al., 2008; Taira et al., 2018) resulting from high pore pressures associated with earthquakes. The changes in elastic wave velocity and permeability from Stage I to II (Figure 4a and b) are in good agreement with observations after earthquakes (Xue et al., 2013; Nimiya et al., 2017). Under Stage II conditions, a resistivity change of ~10–20% (Park, 1991) corresponds to a stress perturbation of 0.2–1.4 MPa, and a permeability change of ~30–40% (Xue et al., 2013) corresponds to a stress perturbation of 0.9–3.2 MPa. Moreover, during Stage II seismic velocity is nearly constant after healing stabilizes the mechanical properties of faults (Nimiya et al., 2017). Nevertheless, subsurface fracture flow could be changing because our results show that seismic velocity is insensitive to pressure above σ_{MPT}. Fault healing eventually leads to large areas of little or no flow (Stages II and III), where mineral precipitation is favored. Pore pressure changes following earthquakes, triggered by several mechanisms such as mineral precipitation (Sibson, 1992; Tenthorey et al., 2003), lead rapidly to decreases in seismic velocity, increases in permeability and decreases in resistivity, after which all of these properties recover (Taira et al., 2018; Xue et al., 2013; Mazzella & Morrison, 1974), which suggests that fracture flow patterns return to their initial condition (Stage I). Thus our inferred transitions in the fracture flow pattern may explain how the cycle of earthquake recurrence is correlated with geophysical observations, complementing the fault-valve model (Sibson et al., 1988).

The other application involves the changes in productivity of fluid resources in fractured reservoirs (for example, geothermal reservoirs) during development. Because increased elastic wave velocity coincides with decreased permeability during Stage I, a gradual velocity increase in geothermal fields implies a slight decrease in reservoir permeability (Taira et al., 2018). If a point is reached where velocity remains steady while resistivity decreases, the fracture flow pattern would be at Stage II or III, where the flow area considerably shrinks. A limited flow area could lead to poorer thermal performance during a geothermal development (Hawkins et al., 2018) and could lower reservoir permeability by as much as two orders of magnitude (Figure 1).

To apply our results to real field locations, we need to consider the scale dependencies of rock properties. For example, although longer fracture lengths generally mean higher roughness values (Brown & Scholtz, 1985; Power et al., 1987; Power & Durham, 1997), fracture permeability in joints is only partially dependent on fracture length (Ishibashi et al., 2015). This suggests that roughness-independent properties such as resistivity (Figure 4b) may have a weak dependence on fracture length, thus resistivity monitoring could be effective for detecting changes in hydraulic

properties at field scale. On the other hand, elastic wave velocity is a roughness-dependent property (Figure 4a) and thus varies with the fracture scale. However, this scaling effect on velocity can be modified by considering the ratio of the wavelength and the fracture length (Mavko et al., 2009). Although our study adopted a low-frequency limit for the velocity calculation, the scaling effect on velocity can be addressed by considering finite wavelengths. Because finite-difference time-domain modeling of wave fields in fractured media requires more complex assumptions, such as fracture compliance (Bakulin et al., 2000; Minato & Ghose, 2016; Pylak-Nolte et al., 1990), the scale dependency on velocity needs to be further explored.

4 Conclusions

We investigated the correlated changes in hydraulic, electrical and elastic properties of joints under increasing normal stress. We found that changes in permeability and resistivity are controlled by fluid connectivity, which is more dependent on stress than on fracture roughness. The relationship between hydraulic and electrical properties is independent of roughness, owing to the roughness independence of fluid connectivity (as expressed by the hydraulic percolation threshold). The roughness dependence of elastic wave velocity arises from the changing distribution of contacting asperities as well as the roughness dependency of porosity. These relationships show promise for improving geophysical interpretations. Our lattice Boltzmann fluid flow simulation revealed that the fracture flow pattern undergoes transitions through three stages as effective normal stress increases: aperture-dependent flow (Stage I), aperture-independent flow (Stage II) and disconnected flow (Stage III). Velocity may be a useful indicator of the Stage I–II transition, and resistivity may be a sensitive indicator of the Stage II–III transition. The relationships we have revealed may enable geological regimes associated with stress changes, such as seismogenic zones and geothermal reservoirs, to be monitored remotely on the basis of their geophysical properties.

Acknowledgments

Authors acknowledge to Dr. I. Katayama and Mr. K. Yamada (Hiroshima University) for the fruitful discussions and conducting the velocity measurement. This work also benefitted from discussions with Dr. T. Ikeda and Dr. J. Nishijima (Kyushu University). The present study was supported in part by the Japan Society for the Promotion of Science (JSPS) through a Grant-in-Aid for JSPS Fellows, 19J10125 (to K.S.) and Grant-in-Aid for Young Scientists, 19K15100 (to F.J.). All results are summarized in Supporting information. The digital fracture data are available online from http://geothermics.mine.kyushu-u.ac.jp/sawayama/grl2020 and from Digital Rocks Portal (http://www.digitalrocksportal.org/projects/273).

References

Ahrenholz, B., Tölke, J., Lehmann, P., Peters, A., Kaestner, A., Krafczyk, M., & Durner, W. (2008). Prediction of capillary hysteresis in a porous material using lattice-Boltzmann methods and comparison to experimental data and a morphological pore network model. *Adv. Water. Resour., 31*(9), 1151–1173, doi:10.1016/j.advwatres.2008.03.009.

Andrä, H., Combaret, N., Dvorkin, J., Glatt, E., Han, J., Kabel, M., et al. (2013). Digital rock physics benchmarks—part II: Computing effective properties. *Comput. Geosci., 50*, 33–43, doi:10.1016/j.cageo.2012.09.008.

Bakulin, A., Grechka, V., & Tsvankin, I. (2000). Estimation of fracture parameters from reflection seismic data—Part II: Fractured models with orthorhombic symmetry. *Geophysics, 65*(6), 1803–1817, doi:10.1190/1.1444864.

Brace, W. F., & Orange, A. S. (1968). Electrical resistivity changes in saturated rocks during fracture and frictional sliding. *J. Geophys. Res., 73*(4), 1433-1445, doi:10.1029/JB073i004p01433.

Brown, S. R. (1989). Transport of fluid and electric current through a single fracture. *J. Geophys. Res., 94*(B7), 9429–9438, doi:10.1029/JB094iB07p09429.

Brown, S. R., & Scholz, C. H. (1985). Broad bandwidth study of the topography of natural rock surfaces. *J. Geophys. Res., 90*(B14), 12575–12582, doi:10.1029/JB090iB14p12575.

Brenguier, F., Campillo, M., Hadziioannou, C., Shapiro, N. M., Nadeau, R. M., & Larose, E. (2008). Postseismic Relaxation Along the San Andreas Fault at Parkfield from Continuous Seismological Observations. *Science, 321*(5895), 1478–1481, doi:10.1126/science.1160943.

Chen, Y., Liang, W., Lian, H., Yang, J., & Nguyen, V. P. (2017). Experimental study on the effect of fracture geometric characteristics on the permeability in deformable rough-walled fractures. *Int. J. Rock. Mech. Min. Sci., 98*, 121–140, doi:10.1016/j.ijrmms.2017.07.003.

Didana, Y. L., Heinson, G., Thiel, S., & Krieger, L. (2017). Magnetotelluric monitoring of permeability enhancement at enhanced geothermal system project, *Geothermics, 66*, 23–38, doi:10.1016/j.geothermics.2016.11.005.

Garboczi, E.J., (1998). Finite element and finite difference programs for computing the linear electric and elastic properties of digital image of random materials. *Natl. Inst. Stand. Technol. Interag. Rep.*, 6269.

Guéguen, Y. & Palciauskas, V. (1994). *Introduction to the physics of rocks*., 294pp., Princeton, NJ: Princeton University Press.

Guéguen, Y., Chelidze, T., & Le Ravalec, M. (1997). Microstructures, percolation thresholds, and rock physical properties. *Tectonophysics, 279*(1–4), 23–35, doi:10.1016/S0040-1951(97)00132-7.

Hawkins, A. J., Becker, M. W., & Tester, J. W. (2018). Inert and Adsorptive Tracer Tests for Field Measurement of Flow-Wetted Surface Area. *Water Resour. Res., 54*(8), 5341–5358, doi:10.1029/2017WR021910.

He, X., & Luo, L.-S. (1997). Lattice Boltzmann Model for the Incompressible Navier–Stokes Equation. *J. Stat. Phys., 88*(3–4), 927–944, doi:10.1023/B:JOSS.0000015179.12689.e4.

Ishibashi, T., Watanabe, N., Hirano, N., Okamoto, A., & Tsuchiya, N. (2015). Beyond-laboratory-scale prediction for channeling flows through subsurface rock fractures with heterogeneous aperture distributions revealed by laboratory evaluation. *J. Geophys. Res. Solid Earth, 120*(1), 106–124, doi:10.1002/2014JB011555.

Jiang, F., Tsuji, T., & Hu, C. (2014). Elucidating the Role of Interfacial Tension for Hydrological Properties of Two-Phase Flow in Natural Sandstone by an Improved Lattice Boltzmann Method. *Transp, Porous Media, 104*(1), 205–229, doi:10.1007/s11242-014-0329-0.

Kinoshita, C., Kano, Y., & Ito, H. (2015). Shallow crustal permeability enhancement in central Japan due to the 2011 Tohoku earthquake. *Geophys. Res. Lett., 42*(3), 773–780, doi:10.1002/2014GL062792.

Kirkby, A., Heinson, G., & Krieger, L. (2016). Relating permeability and electrical resistivity in fractures using random resistor network models. *J. Geophys. Res. Solid Earth, 121*(3), 1546–1564, doi:0.1002/2015JB012541.

Mavko, G., Mukerji, T. & Dvorkin, J. (2009). *The Rock Physics Handbook: Tools for Seismic Analysis of Porous Media*. 2nd ed., 511pp., Cambridge, U.K.: Cambridge University Press.

Mazzella, A., & Morrison, H. F. (1974). Electrical Resistivity Variations Associated with Earthquakes on the San Andreas Fault. *Science*, *185*(4154), 855–857, doi:10.1126/science.185.4154.855.

Minato, S., & Ghose, R. (2016). Enhanced characterization of fracture compliance heterogeneity using multiple reflections and data-driven Green's function retrieval. *J. Geophys. Res. Solid Earth, 121*(4), 2813–2836, doi:10.1002/2015JB012587.

Nemoto, K., Watanabe, N., Hirano, N., & Tsuchiya, N. (2009). Direct measurement of contact area and stress dependence of anisotropic flow through rock fracture with heterogeneous aperture distribution. *Earth Planet. Sci. Lett., 281*(1–2), 81–87, doi:10.1016/j.epsl.2009.02.005.

Nimiya, H., Ikeda, T., & Tsuji, T. (2017). Spatial and temporal seismic velocity changes on Kyushu Island during the 2016 Kumamoto earthquake. *Sci. Adv., 3*(11), e1700813, doi:10.1126/sciadv.1700813.

Park, S. K. (1991). Monitoring resistivity changes prior to earthquakes in Parkfield, California, with telluric arrays. *J. Geophys. Res. Solid Earth, 96*(B9), 14211–14237, doi:10.1029/91JB01228.

Paterson, M. S. & Wong, T. (2005). *Experimental Rock Deformation: The Brittle Field*. 2nd ed., 347pp., New York, NY: Springer-Verlag.

Peacock, J. R., Thiel, S., Heinson, G. S., & Reid, P. (2013). Time-lapse magnetotelluric monitoring of an enhanced geothermal system. *Geophysics, 78*(3), B121–B130, doi:10.1190/geo2012-0275.1.

Peacock, J. R., Thiel, S., Reid, P., & Heinson, G. (2012). Magnetotelluric monitoring of a fluid injection: Example from an enhanced geothermal system. *Geophys. Res. Lett., 39*(18), 3–7, doi:10.1029/2012GL053080.

Power, W. L., & Durham, W. B. (1997). Topography of natural and artificial fractures in granitic rocks: Implications for studies of rock friction and fluid migration. *Int. J. Rock Mech. Min. Sci., 34*(6), 979–989,doi:10.1016/S1365-1609(97)80007-X.

Power, W. L., Tullis, T. E., Brown, S. R., Boitnott, G. N., & Scholz, C. H. (1987). Roughness of natural fault surfaces. *Geophys. Res. Lett., 14*(1), 29–32, doi:10.1029/GL014i001p00029.

Pyrak-Nolte, L. J., & Nolte, D. D. (2016). Approaching a universal scaling relationship between fracture stiffness and fluid flow. *Nat. Commun., 7*(1), 10663, doi:10.1038/ncomms10663.

Pyrak-Nolte, L. J., Myer, L. R., & Cook, N. G. W. (1990). Transmission of seismic waves across single natural fractures. *J. Geophys. Res., 95*(B6), 8617–8638, doi:10.1029/JB095iB06p08617.

Raven, K. G., & Gale, J. E. (1985). Water flow in a natural rock fracture as a function of stress and sample size. *Int. J. Rock. Mech. Min. Sci. & Geomech. Abstr., 22*(4), 251–261, doi:10.1016/0148-9062(85)92952-3.

Sain, R., Mukerji, T., & Mavko, G. (2014). How computational rock-physics tools can be used to simulate geologic processes, understand pore-scale heterogeneity, and refine theoretical models. *Lead. Edge, 33*(3), 324–334, doi:10.1190/tle33030324.1.

Saxena, N., & Mavko, G. (2016). Estimating elastic moduli of rocks from thin sections: Digital rock study of 3D properties from 2D images. *Comput. Geosci., 88*, 9–21, doi:10.1016/j.cageo.2015.12.008.

Scholz, C. H. (2002). *The mechanics of earthquakes and faulting*. 2nd ed., 471pp., Cambridge, U.K.: Cambridge University Press.

Sibson, R. H. (1992). Implications of fault-valve behaviour for rupture nucleation and recurrence. *Tectonophysics, 211*(1–4), 283–293, doi:10.1016/0040-1951(92)90065-E.

Sibson, R. H., Robert, F., & Poulsen, K. H. (1988). High-angle reverse faults, fluid-pressure cycling, and mesothermal gold-quartz deposits. *Geology, 16*(6), 551–555, doi:10.1130/0091-7613(1988)016<0551:HARFFP>2.3.CO;2.

Taira, T., Nayak, A., Brenguier, F., & Manga, M. (2018). Monitoring reservoir response to earthquakes and fluid extraction, Salton Sea geothermal field, California. *Sci. Adv., 4*(1), e1701536, doi:10.1126/sciadv.1701536.

Tenthorey, E., Cox, S. F., & Todd, H. F. (2003). Evolution of strength recovery and permeability during fluid–rock reaction in experimental fault zones. *Earth Planet. Sci. Lett., 206*(1–2), 161–172, doi:10.1016/S0012-821X(02)01082-8.

Tsuji, T., Ikeda, T., & Jiang, F. (2019). Evolution of hydraulic and elastic properties of reservoir rocks due to mineral precipitation in CO_2 geological storage. *Comput. Geosci., 126*, 84–95, doi:10.1016/j.cageo.2019.02.005.

Tsuji, T., Tokuyama, H., Costa Pisani, P., & Moore, G. (2008). Effective stress and pore pressure in the Nankai accretionary prism off the Muroto Peninsula, southwestern Japan. *J. Geophys. Res, 113*(B11), B11401, doi:10.1029/2007JB005002.

Vogler, D., Settgast, R. R., Annavarapu, C., Madonna, C., Bayer, P., & Amann, F. (2018). Experiments and simulations of fully hydro-mechanically coupled response of rough fractures exposed to high-pressure fluid injection. *J. Geophys. Res. Solid Earth,123*(2), 1186–1200, doi:10.1002/2017JB015057.

Wang, L., & Cardenas, M. B. (2016). Development of an empirical model relating permeability and specific stiffness for rough fractures from numerical deformation experiments. *J. Geophys. Res. Solid Earth,121*(7), 4977–4989, doi:10.1002/2016JB013004.

Watanabe, N., Hirano, N., & Tsuchiya, N. (2008). Determination of aperture structure and fluid flow in a rock fracture by high-resolution numerical modeling on the basis of a flow-

through experiment under confining pressure. *Water Resour. Res., 44*(6), 1–11, doi:10.1029/2006WR005411.

Xue, L., Li, H.-B., Brodsky, E. E., Xu, Z.-Q., Kano, Y., Wang, H., et al. (2013). Continuous Permeability Measurements Record Healing Inside the Wenchuan Earthquake Fault Zone. *Science, 340*(6140), 1555–1559, doi:10.1126/science.1237237.

Zimmerman, R. W., Chen, D.-W., & Cook, N. G. W. (1992). The effect of contact area on the permeability of fractures. *J. Hydrol., 139*(1–4), 79–96, doi:10.1016/0022-1694(92)90196-3.

Table 1. Physical properties used for finite-element modeling of resistivity and elastic wave velocity.

	Conductivity [mS/m]	Bulk modulus [GPa]	Shear modulus [GPa]	Density [kg/m^3]
Solid	0.01*	66.3***	32.1***	2750
Fluid	5000**	2.25	0	993

* Based on the experimental result of the resistivity measurement under dry condition
** For seawater
*** Based on P- and S-wave velocity measurements under dry conditions and high confining pressure (200 MPa)

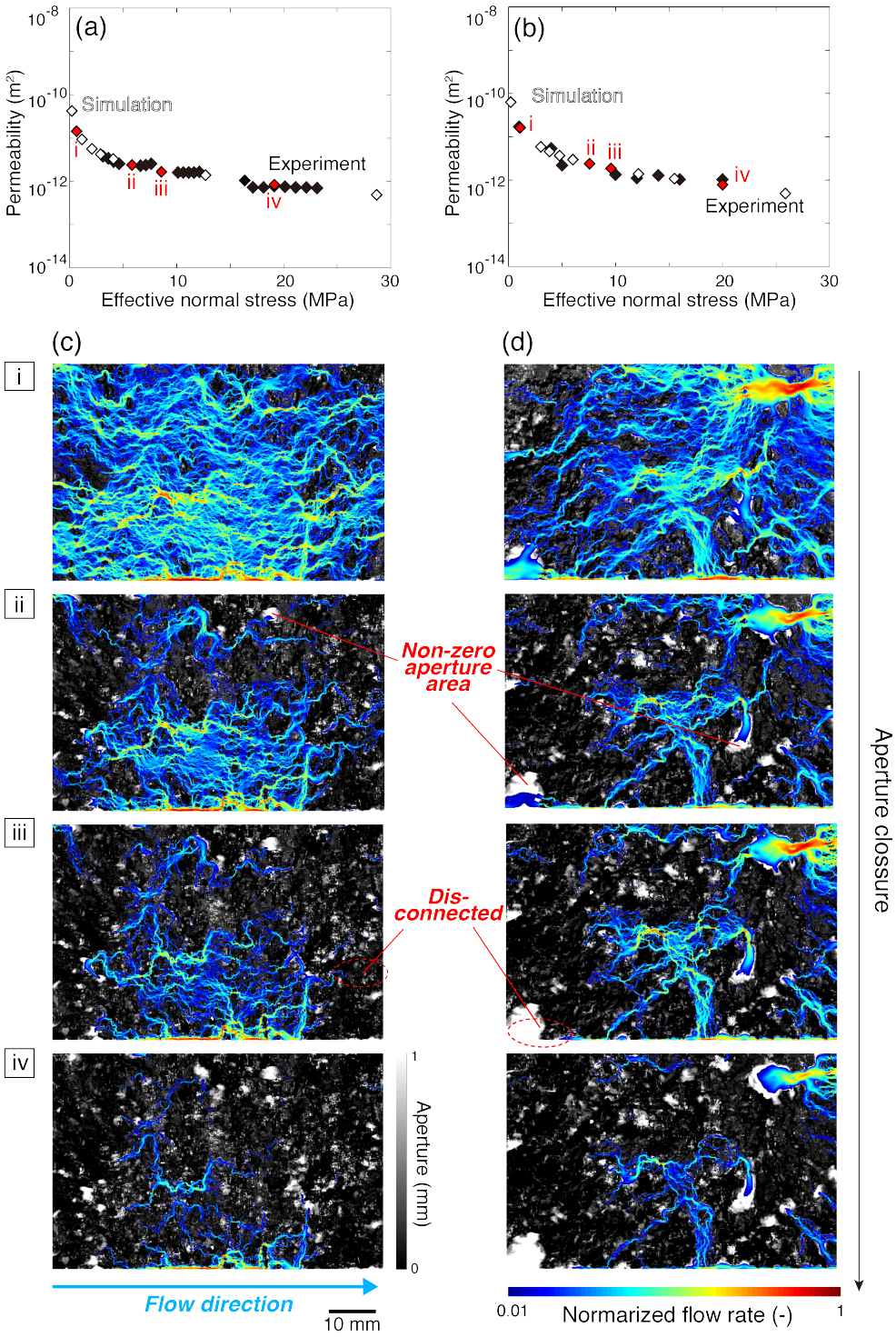

Figure 1. Experimental and simulated fracture permeabilities with increasing effective normal stress of the (a) smooth and (b) rough fractures and representative images derived from the simulation showing fracture flow distribution (color) within the heterogeneous aperture distribution (grayscale) with aperture closure of the (c) smooth and (d) rough fractures. Black and white diamonds in (a) and (b) represent experimental and simulated results, respectively. Red diamonds in (a) and (b) are the representative results that are illustrated in (c) and (d).

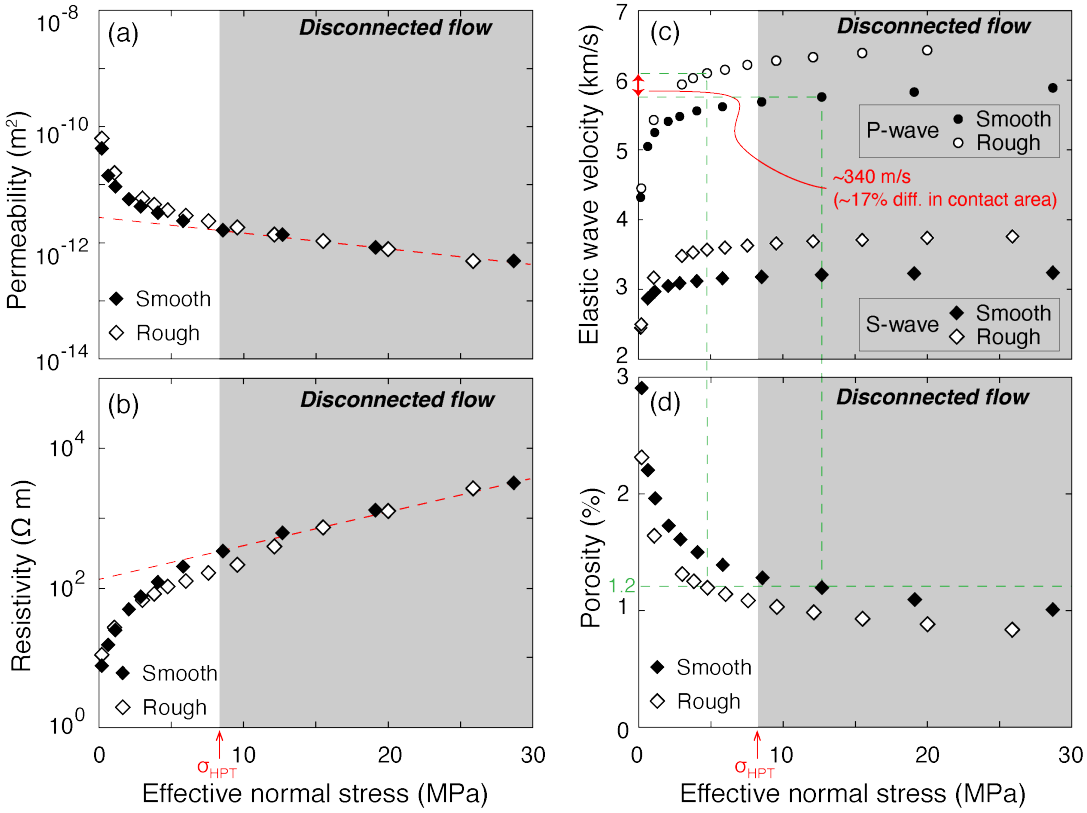

Figure 2. Graphs showing changes in (a) permeability, (b) resistivity, (c) elastic wave velocity and (d) porosity in relation to effective normal stress. Red dashed lines are extrapolations from the data in the regions of disconnected flow (gray), as defined by the value of σ_{HPT}.

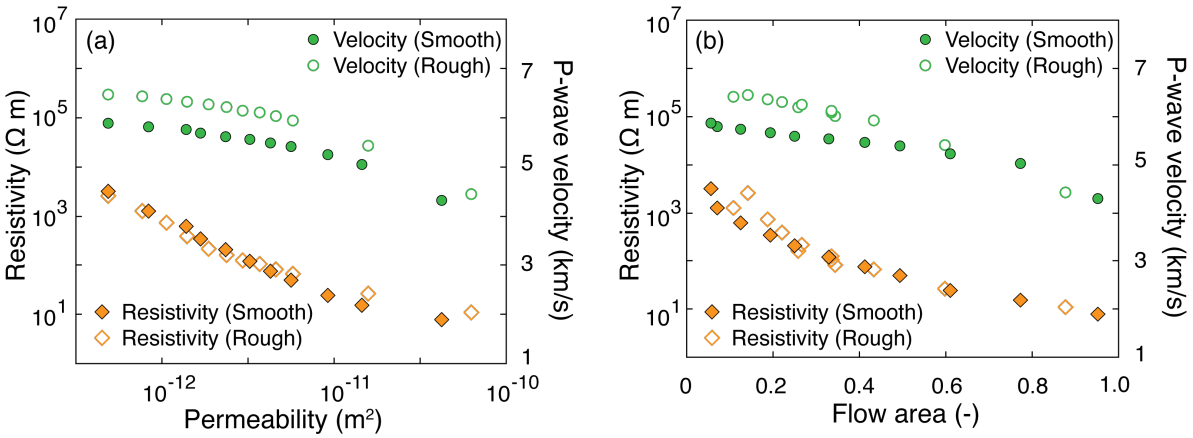

Figure 3. Graphs showing correlations between (a) permeability and geophysical properties and (b) flow area and geophysical properties. Orange and green symbols represent resistivity and P-wave velocity, respectively, and open and solid symbols represent smooth and rough fractures, respectively.

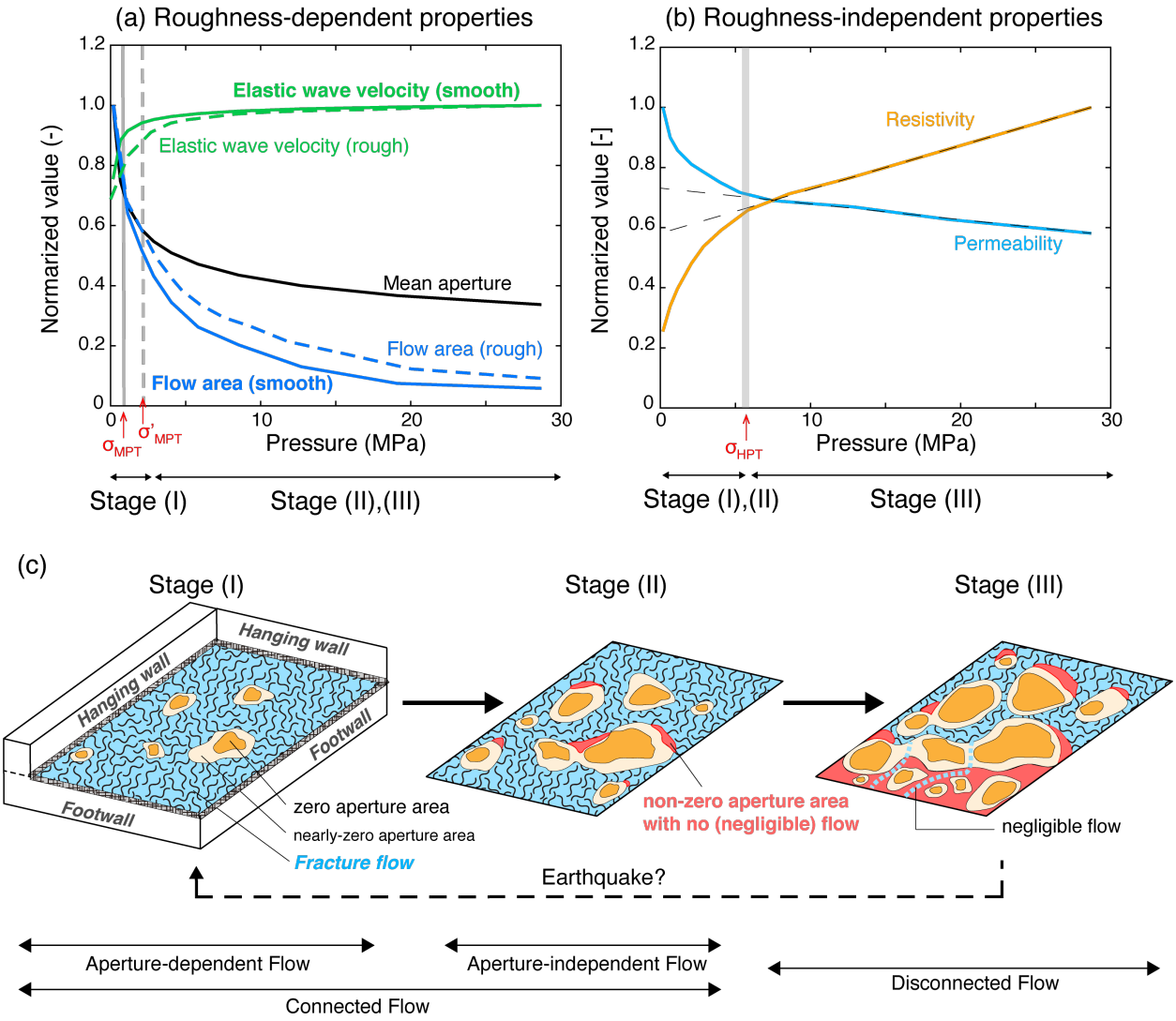

Figure 4. Schematic diagram of changes with respect to pressure in (a) roughness-dependent properties and (b) roughness-independent properties and (c) schematic images of the three-stage transition of fracture flow patterns. All rock physical properties in (a) and (b) are normalized based on our results. Gray lines in (a) represent mechanical percolation thresholds σ_{MPT} and σ'_{MPT} of smooth and rough fractures, respectively, which distinguish aperture-dependent and aperture-independent flows (Stages I and II). The gray line in (b) represents the hydraulic percolation threshold σ_{HPT}, which represents the boundary between connected flow (Stages I and II) and disconnected flow (Stage III).